Hong, Yang, Han, Dan, Hou, Bo , Wang, Xinyu and Zhang, Jingchao 2021. High-throughput computations of cross-plane thermal conductivity in multilayer stanene. International Journal of Heat and Mass Transfer 171 , 121073. 10.1016/j.ijheatmasstransfer.2021.121073

High-Throughput Computations of Cross-Plane Thermal Conductivity in Multilayer Stanene

Yang Hong[1], Dan Han[2], Bo Hou[3], Xinyu Wang[2,*], Jingchao Zhang[4,*]

[1]School of Chemistry and Biochemistry, Georgia Institute of Technology, Atlanta, GA 30332, USA

[2]Institute of Thermal Science and Technology, Shandong University, Jinan 250061, China

[3]Department of Physics and Astronomy, Cardiff University, Cardiff CF24 3AA, UK

[4]Department of Biostatistics and Bioinformatics, Emory University, Atlanta, GA 30322, USA

ABSTRACT

Computational materials science based on data-driven approach has gained increasing interest in recent years. The capability of trained machine learning (ML) models, such as an artificial neural network (ANN), to predict the material properties without repetitive calculations is an appealing idea to save computational time. Thermal conductivity in single or multilayer structure is a quintessential property that plays a pivotal role in electronic applications. In this work, we exemplified a data-driven approach based on ML and high-throughput computation (HTC) to investigate the cross-plane thermal transport in multilayer stanene. Stanene has attracted considerable attention due to its novel electronic properties such as topological insulating features with a wide bandgap, making it an appealing candidate to ferry current in electronic devices. Classical molecular dynamics simulations are performed to extract the lattice thermal conductivities (κ_L). The calculated cross-plane κ_L is orders of magnitude lower than its lateral counterparts. Impact factors such as layer number, system temperature, interlayer coupling strength, and compressive/tensile strains are explored. It is found that κ_L of multilayer stanene in the cross-plane direction can be diminished by 86.7% with weakened coupling strength, or 66.6% with tensile strains. A total of 2700 κ_L data are generated using HTC, which are fed into 9 different ANN models for training and testing. The best prediction performance is given by the 2-layer ANN with 30 neurons in each layer.

---

[*] Corresponding authors. Xinyu Wang: xyw@sdu.edu.cn; Jingchao Zhang: jingchao.zhang@emory.edu.

1. Introduction

Machine learning (ML) has gained increasing popularity in various fields such as natural language processing, image classification, self-driving automobiles and medical diagnosis.[1-4] In recent years, with the help of high clock speed central processing unit and acceleration hardware such as graphical process unit, the application of ML models in computational materials science has become possible. High-throughput computations (HTC) combined with numerical approaches such as first-principles and molecular dynamics (MD) simulations have enabled the fast generations of training dataset for supervised ML models. Artificial neural network (ANN) is an important branch of machine learning and become dominant in many fields owing to its capabilities of learning complex correlations in large dataset. Several attempts have been made to predict materials properties with ANN. Using a convolutional neural network (CNN), the thermal conductivities of composite materials have been successfully predicted with image-based training data.[5] The interfacial thermal resistance between graphene and hexagonal boron nitride has been successful models using a fully connected feed-forward neural network.[6] In a recent study, a recurrent neural network (RNN) has been employed to accelerate the simulation clock of *Ab initio* molecular dynamics.[7] Using a machine-learning interatomic potential, Mortazavi et al.[8] calculated the lattice thermal conductivity of graphene/borophene heterostructures. The machine-learning interatomic potentials (MLIPs) is trained on ab initio molecular dynamics (AIMD) trajectories which preserves the accuracy of the first-principles approaches while achieves faster calculations superior than classical molecular dynamics (MD) simulations. This MLIPs have also been used to predict other 2D materials such as nanoporous C_3N_4, C_3N_5 and C_3N_6 nanosheets.[9-11] Other types of machine learning based potentials have also been developed to predict the thermal properties of MnxGey compounds,[12] silicon,[13] silicene,[14] WSe_2,[15] and $MoS_{2(1-x)}Se_{2x}$[16].

Stanene, a newly discovered 2D monolayer of Sn atoms arranged in corrugated hexagonal patterns, has spurred extensive experimental investigations due to their topological insulating behavior with a very large bandgap, as well as near room-temperature quantum Hall effect.[17-20] Recently, the fabrication of monolayer stanene has been achieved by using a molecular beam epitaxy method.[21] The successful synthesis of stanene further stimulates more experimental and numerical studies of its novel properties. A doped stanene film is a good candidate for 2D topological superconductor.[22] When the inter-orbital attractive interaction within decorated stanene is escalated over the intra-orbital interaction, topological superconductivity can be achieved with the final state in monolayer stanene. Moreover, unprecedented high thermoelectricity with a figure of merit (*ZT*) of 7 is realized in stanene by geometry optimization.[17] In practical applications, high thermal conductivity (κ) materials such as graphene can be utilized as thermal interface materials (TIMs) to facilitate heat dissipations in electronic devices. Aside from graphene, several high thermal conductivity materials such as C_3N[23] and graphene-based heterobilayers[24-27] have been proposed as possible thermal interface materials. On the other hand, the ultra-low thermal conductivity may serve as a promising solution to enhance thermoelectric devices figure of merit, which is expressed as $ZT = S^2\sigma T/(\kappa_e + \kappa_L)$, where S is the Seebeck coefficient, σ is the electrical conductivity, T is the absolute temperature, and κ_e, κ_L represent electronic and lattice thermal conductivity, respectively. The enhancement of thermoelectric properties requires the improvement of conflicting properties. For example, high *ZT* values require low phonon thermal transport and high electrical conductivities.[28] Electronic thermal transport normally has positive correlations with electrical conductivity. Understanding the electron and phonon transport properties in stanene is therefore highly important to further exploit its potentials in thermoelectric applications.

Thermal transport in monolayer stanene has been investigated by several numerical studies. By solving the phonon Boltzmann equation combined with density functional theory (DFT) calculations, the in-plane lattice thermal conductivities of stanene along zigzag and armchair directions are calculated as 10.8 and 9.2 W/m·K, respectively.[29] In a similar study, Peng *et al.*[30] predicted that the lattice thermal conductivity of stanene equals 11.6 W/m·K with dominant contributions from high-group-velocity longitudinal acoustic (LA) phonons. Using the equilibrium molecular dynamics (EMD) method, Cherukara *et al.*[31] calculated the thermal conductivity of stanene in the armchair and zigzag directions to be 6.5 ± 0.5 and 6.4 ± 0.3 W/m·K at 300 K. They also concluded that the specific heat of stanene reaches 90% of its classical limit at 100 K, which gives negligible differences between classical and quantum phonon populations at temperatures above this value. Therefore, quantum correction is not needed when calculating the thermal properties of stanene at temperatures greater than 100 K. Despite the studies on the in-plane thermal properties of stanene, its cross-plane thermal conductivity remains unexplored and an open topic.

In this work, a data-driven approach based on machine learning and high-throughput computation is used to investigate the lattice thermal conductivity of multilayer stanene (MLS). The effects of layer number, system temperature, interlayer coupling strength and external strains on the predicted thermal conductivity are evaluated. The phonon properties of stanene are investigated by exploring its phonon density of states (PDOS) and phonon spectral energy density (SED). This paper is organized as follows. Section 2 details the MD simulation setup and machine learning principles. Section 3 discusses the effects of each modulator on the predicted cross-plane thermal conductivity with corresponding discussions, followed by the ANN model training and prediction results. The last section summarizes the results reported in this work.

2. Machine Learning Algorithm and Atomic Modeling

All MD simulations are performed by the open-source package Large-scale Atomic/Molecular Massively Parallel Simulator (LAMMPS).[32] Atom configurations of the stacked stanene layers are shown in Fig. 1(a). Periodic boundary conditions are used in the in-plane directions and free boundary is used in the out-of-plane direction. The initial distance between neighboring stanene layers is set as 4.92 Å. The steady-state distance after relaxation is 3.81 Å at temperature 300 K. The Tersoff potential is used to model the Sn-Sn interactions within stanene monolayer.[31] This potential has been widely applied in thermal property calculations of stanene monolayers and heterostructures.[33-36] To further valid the empirical potential used in this work, in-plane thermal conductivity of stanene are calculated using non-equilibrium molecular dynamics (NEMD) simulation and compared to first-principles result. Five different system lengths of 20.1, 40.5, 81.3, 162.8 and 325.9 nm are used in the calculations. The system width is fixed at 4.7 nm for all cases. Periodic boundary condition is used in the width direction and free boundary conditions are used in the heat flux and out-of-plane directions. After 200 ps NVT and 50 ps NVE calculations, a heat flux of 1×10^9 W/m^2 is imposed to the system for 4 ns before data collections. Each lattice thermal conductivity is averaged from three independent simulations with different initial conditions. The calculated κ is shown in Fig. S1(a) and the inversion correlation between system length and thermal conductivity is shown in Fig. S1(b). The calculated thermal conductivity at different lengths coincides well with previous MD simulations.[37, 38] The predicted in-plane lattice thermal conductivity for single-layer infinite length stanene is 8.3 W/m·K, which is very close to the first-principles predicted result of 9.2 W/m·K.[29] This further justifies the usage of the current empirical potential in this work. Interactions between the stanene layers are described by the 12-6 Lennard-Jones (LJ) potential

$$V(\mathrm{r}) = 4\chi\varepsilon[(\frac{\sigma}{r})^{12} - (\frac{\sigma}{r})^{6}], \tag{1}$$

where σ, ε and r represent the zero-potential distance, potential well depth and interatomic distance, respectively. The interlayer coupling strength is adjusted by a parameter χ. The LJ parameters are calculated based on the universal force field (UFF),[39] where $\varepsilon_{\text{Sn–Sn}} = 24.621$ meV and $\sigma_{\text{Sn–Sn}} = 3.913$ Å. The cutoff distance r_c equals $3.5 \times \sigma_{\text{Sn–Sn}}$, which is 13.7 Å.

The cross-plane thermal conductivity is calculated by the NEMD method, which has been widely used in thermal property characterizations.[40-46] At steady state, the atomic velocities should follow the Maxwell–Boltzmann (MB) distribution

$$P = 4\pi v^2 \left(\frac{m}{2\pi k_B T} \right)^{3/2} e^{-mv^2/2k_B T}, \tag{2}$$

where T is system temperature, m represents atomic mass and P is the probability of an atom with velocity v. The MB distribution is used to verify that the MLS system has reached steady state before data collections. The velocity distributions before and after the NEMD process are shown in Fig. 1(b). To further confirm that the system has reached steady state before data collection, the same system is used for heat flux calculations. The heat flux along the heat transfer direction is shown in Fig. S2. It can be observed that the heat flux is constant during data collection, which is consistent with the velocity distribution results. Time step is 0.5 fs for all calculations. The outermost layers of the system in the z-direction are selected as the heat source and heat sink respectively. The initial structure is first placed under a canonical ensemble (NVT) for 300 ps and then switched to a microcanonical ensemble (NVE) for another 200 ps. After thermal equilibrium calculations, a constant heat flux $\dot{q}$ is imposed on the system continuously for 1.5 ns. The temperature distribution at steady-state is shown in Fig. 1(c). Based on the Fourier's law of heat conduction, thermal conductivity κ_L can be calculated from $\kappa_L = -\dot{q}/\nabla T$, where ∇T is the temperature gradient extracted from linear fitting. For each data point, five independent simulations with different initial velocity configurations are performed and the average value is used as the final result.

To gain further insights into the phonon behaviors, phonon power spectrum analyses are performed on monolayer stanene for transverse (TA), longitudinal (LA) and flexural phonons (ZA) respectively. The PDOS can be calculated by taking the Fourier transform of the velocity autocorrelation function

$$G(\omega) = 1/\sqrt{2\pi}\int_0^{\infty} < v(0)\cdot v(\mathrm{t}) > / < v(0)\cdot v(0) > e^{i\omega t}dt \,. \tag{3}$$

The different phonon behaviors of freestanding and supported stanene can be revealed by phonon spectral energy density (SED) analyses based on equation[47]

$$\phi(k,\omega) = \frac{m}{4\pi N\tau}\sum_{\alpha}\sum_{b}^{B}\left|\int_0^{\tau}\sum_{n_{x,y,z}}^{N}\dot{v}_{\alpha}(\genfrac{}{}{0pt}{}{n_{x,y,z}}{b};t)\exp[ik\cdot r(\genfrac{}{}{0pt}{}{n_{x,y,z}}{0})-i\omega t]dt\right|^2 , \tag{4}$$

where m is atomic mass, B is the number of atoms in a unit cell, N is the number of unit cells, τ is the integration time, α is the integration direction (x, y, z), $\dot{v}_{\alpha}$ is the velocity of atom b in unit cell $n_{x,y,z}$ at time step t, and r is the equilibrium position of unit cell $n_{x,y,z}$.

Artificial neural network is the state-of-the-art machine learning approach and can be formed into advanced architectures that effectively capture complex features given enough data and computation. A typical artificial neural network is composed of one input layer, one output layer and one or more hidden layers. A schematic of a fully connected feed-forward ANN is shown in Fig. 1(d). The input layer is represented by the red circles, where each circle represents a feature value. In this work, impact factors such as layer number, system temperature, interlayer coupling strength and external strain are used as feature values. The green circles in the hidden layers represent neurons whose bias and weight terms will be optimized according to a loss function. The objective of the model training is to minimize the loss function and achieve a global minimum. Since the calculated thermal conductivity values are continuous numeric values, the mean square error (MSE) is used as the loss function, which is expressed as:

$$Loss(\hat{y}, y, W) = \frac{1}{2}\|\hat{y} - y\|^2 + \frac{\alpha}{2}\|W\|^2, \tag{5}$$

where $\hat{y}$ is the predicted value, y is the target value, $\alpha\|W\|^2$ is the L2-regularization term, α is a parameter for the regularization and W is the weight matrix. The purpose of the L2 term is to combat overfitting by constraining the size of the weights. A high α value could fix the high variance problem by enforcing smaller weight values. On the other hand, a small α value loosens the restrictions and leads to more complex decision boundaries. A heuristically-determined α value of 0.0001 is used for ANN models in this work. The weight matrix is learned using a gradient descent method expressed as

$$W^{i+1} = W^{i} - \eta \nabla Loss_{W}^{i}, \tag{6}$$

where i is the learning step and η is the learning rate. A constant learning rate of 0.001 is used in this work. The training procedures are shown in Fig. 1(e). The first step is to setup MD simulations with different input parameters. Three different layer numbers from 8 to 16, five system temperatures from 100 to 500 K, six different coupling strength from 0.5 to 3.0, six different strain values from 0 to 5%, and five different velocity seeds are used to generate the training and test dataset. A total number of 2700 κ_L values is obtained. Once the feature values have been determined, the training dataset is fed into the ANN architecture.

3. Results and Discussion

To characterize the cross-plane thermal conductivity, a 16-layer system with lateral dimensions of 10.0×10.0 (x×y) nm^2 is created. Non-linear temperature distributions near the thermal reservoirs are observed and excluded from the linear fitting process.[48-50] From Fig. 1(b), it can be observed that the velocities extracted from MD simulations match well with the theoretical Maxwell predictions, which indicate the system has reached steady state before NEMD calculation and data collection. The predicted thermal conductivity for 16-layer stanene equals 0.16 W/m·K at temperature 300 K, which is an order of magnitude lower than its in-plane thermal conductivities.[29] Effect of lateral size on the predicted κ_L value is also investigated. A much larger in-plane dimension of 20.3×20.3 (x×y) nm^2 is used and the calculated result is only 0.4% different from the previous result. Therefore, it can be concluded that the κ_L values are converged with lateral dimensions and the smaller value 10.0×10.0 (x×y) nm^2 is selected to save computational cost.

The SED calculation is performed under the NVE ensemble with an integration time step of 0.1 fs for a total simulation time of 100 ps. Snapshots of atom velocities are taken every 200 time steps. The unit cell length a is defined as 4.902 Å. The calculated SED results for freestanding and supported stanene in a bilayer structure are shown in Figs. 2(a) and (b) respectively. Since lattice thermal conductivity is mainly contributed by the lower frequency acoustic phonons, a frequency range of 0-3 THz is selected. The blurred phonon SED in Fig. 2(b) indicated stronger phonon scatterings and thermal conductivity reduction as compared to the freestanding case. It also can be observed in Fig. 2(b) that the phonon modes at k_0 point shifted to higher frequencies in the bilayer structure. Similar results have also been observed in h-BN[51], graphene[52] and silicene[53]. The variation is mainly attributed to the restricted phase space for phonon-phonon scattering in the cross-plane direction and the weak van der Waals (vdW) interactions between stanene monolayers, which could modify the interatomic force constants. The calculated PDOS for stanene is shown in Fig. S3. It can be observed that the active phonon frequency range is from 0-6 THz, which is much smaller than that of graphene.[54] On the other hand, the in-plane LA/TA phonons are anisotropic from the cross-plane ZA phonons, which is similar to that of graphene.[54]

Next, we investigate the dependence of lattice thermal conductivity with layer number. Aside from the 16-layers stanene system, other layer numbers of 8, 12, 24, 32 and 64 are used for κ_L predictions. The calculated lattice thermal conductivity results with layer number are shown in Fig. 2(c). The uncertainty is calculated based on five independent simulations. It can be observed that at small thickness scales, the cross-plane κ_L increases sharply with layer number and gradually converges at large values. The calculated κ_L increases from 0.08 to 0.43 W/m·K when the layer number increases from 8 to 64. Using the EMD method, Ni *et al.*[55] calculated the interfacial thermal resistance (*R*) between a few layer graphene (FLG). It was proved that *R* decreases with increasing layer number in FLG, indicating a positive correlation between layer number and thermal conductivity, which agrees well with our simulations. With an increasing number of stanene layers, the cross-plane phonon couplings are enhanced due to the interactions from farther layers, which as a result will facilitate the thermal transport. To extract the bulk cross-plane lattice thermal conductivity and phonon mean free path (MFP) of stanene, the calculated thermal conductivity results are fitted using a linear function[56]

$$\frac{1}{\kappa_L} = \frac{1}{\kappa_\infty}\left(\frac{l}{L}+1\right), \tag{7}$$

where κ_L is the thermal conductivity at system length *L*, *l* is the effective phonon MFP, and κ_∞ is the thermal conductivity at infinite length. The fitting results for $1/\kappa_L$ and 1/*L* are shown in Fig. 2(d). It can be observed that the linear fitting profile soundly matches the calculated results. The predicted bulk lattice thermal conductivity at the cross-plane direction of MLS is 0.83 W/m·K, which is still an order of magnitude smaller than those in-plane results.[30] When the system size in the heat transfer direction is not significantly larger than the phonon mean free path, the size effect arises. This is a results of phonon scattering between the heat reservoirs.[56] Once the thermal conductivities of multilayer stanene with different layers calculated, it is possible to estimate the MLS thermal conductivity through an extrapolation method. The assumes that the boundary scattering dominates the impeding phonon transport. If the linear relationship exists, the effective thermal conductivity for an infinite layer number stanene can be extrapolated at $1/N = 0$, where N is the layer number of the multilayer graphene. This approach has been widely to extract cross-plane thermal conductivity in multilayer structures. For instance, using classical MD simulation, Chen *et al*.[57] reported a similar phenomenon in multilayer graphene at 48 layers (thickness ~16 nm). Cross-plane thermal conductivities of popular vdW structures are summarized in Table 1.

Based on the previous study, the cross-plane thermal conductivity of multilayer graphene is 11.57 W/m·K, which is much larger than other 2D materials.[58] The dominant phonon wavelength in a multilayer graphene structure is predicted to be 3.45 Å, which is comparable to the thickness of a single-layer graphene. On the other hand, κ_L of multilayer phosphorene in the cross-plane direction is only 0.42 W/m·K.[59] This small κ_L could be attributed to the hinge-like structure in phosphorene, which weakens the surface contact between phosphorene layers and lead to reduced thermal conductivity. Similar to that of phosphorene, the buckled structure of stanene could also lead to low cross-plane thermal conductivities.

The Joule heating during device operations could place the electronic components under various working temperatures and affect their thermophysical properties. One the other hand, surface treatment during electronic device fabrications are often used to modify the material interaction strengths at the interfaces. Therefore, the effects of temperature and interlayer coupling strength on the cross-plane lattice thermal conductivity of MLS are further explored. A temperature range from 100 to 500 K is used. To be consistent with previous calculations, a 16-layer MLS with periodic boundary conditions in lateral directions is selected. The calculated κ_L with temperature is shown in Fig. 3(a). In general, when the crystal temperature increases, phonon Umklapp scattering becomes stronger and the effective phonon MFP is reduced, thus resulting in reduced thermal conductivities. The lattice thermal conductivity of MLS decreases by 71% from 0.28 W/m·K to 0.08 W/m·K when temperature increases from 100 to 500 K. The decreasing trend of κ_L with temperature is also observed in various heterostructures.[36, 60-62] When interlayer coupling strength increases from 0.5 to 3.0, the averaged lattice thermal conductivity is upraised from 0.08 to 0.56 W/m·K. The increase of χ enhances the contact pressure, which directly strengthens the interlayer phonon coupling and reduces the thermal resistance. On the other hand, the enhanced coupling strength can directly heighten the atom interaction of two layers, promoting the lattice synergy vibration and energy transmission across the interface. The increase of cross-plane lattice thermal conductivity with coupling strength has also been observed in previous studies. We further calculate the SED of the bilayer with $\chi = 2$ in comparison with pristine bilayer, which as shown in the Fig. S4. It can be observed in Fig. S4 (b) that the phonon modes at Γ point shift to higher frequencies in the bilayer structure with $\chi = 2$. The phonon relaxation time is obtained by fitting each SED peak to the Lorentzian function as[63]

$$\phi(k,\omega)=\frac{I}{1+\left[2\left(v-v_c\right)/\gamma\right]^2}, \tag{8}$$

$$\tau_p = 1/\gamma, \tag{9}$$

where I is the peak magnitude of the phonon branch, v_c means the peak center frequency, γ is the width at half-maximum and τ_p is the phonon relaxation time. The results of phonon relaxation time for bilayer with pristine and strong coupling strength are shown in Fig. S5. In general, the phonon relaxation times of bilayer with $\chi = 2$ are larger than that of bilayer with $\chi = 1$. To make an intuitive comparison, the average phonon relaxation times of bilayer with $\chi = 1$ and $\chi = 2$ are calculated, which are equal to 1.721 and 1.732

ps, respectively. The larger phonon relaxation time indicates the larger thermal conductivity as the coupling strength increases, which is consistent with our MD results of thermal conductivity under different coupling strength. To directly address the better energy transmission with stronger coupling strength, a bilayer stanene system is constructed with dimensions of 10.0×10.2 (x×y) nm^2. The system is placed under NVT at temperature 300 K to reach thermal equilibrium, followed by a 100 of NVE relaxation. Then a pulsed heat was imposed on the top layer for 50 fs to increase the temperature to around 600 K. Due to the temperature difference between the top and bottom layers, thermal energy will flow from the high temperature region to the lower one. In this isolated system, the only thermal pathway is the energy transmission at the interface. Thermal relaxation is performed for another 100 ps and the temperatures of the top and bottom stanene layers are plotted in Fig. S6. It can be observed that when the coupling strength increases, the time used for temperature convergence decreases, which roughly equals 40, 20 and 10 ps for $\chi = 2$, $\chi = 1$ and $\chi = 0.5$, respectively. Prasher *et al.*[64] calculated the thermal contact resistance of vdW interfaces using an acoustic mismatch model which indicates the same conclusion that thermal conductance increases with bonding strength. Such effects are similar to the pressure-induced thermal transport enhancement at the material interface and in polymers.[65] The atom distance is smaller when higher pressure is applied which enhances the energy transport efficiency from one to another.

Surface materials are often deformed to fit in with the substrate's topological structures to achieve optimal performances. Layer distance variations induced by external strains can bring unexpected alterations to the material's electrical and thermal properties. In this work, the effects of tensile and compressive strains on the cross-plane thermal conductance of MLS are explored. The definition of strain is $\lambda = (l - l_0)/l_0$, where l and l_0 stand for strained and initial system lengths respectively. To be consistent with previous calculations, the 16-layer MLS is selected with $T = 300$ K, $\chi = 1.0$ and $\dot{q} = 1.6 \times 10^9$ W/m^2. After thermal equilibrium calculations, external forces in the cross-plane direction are directly exerted on the outermost layers of stanene continuously for 500 ps. The corresponding component of force is added on each atom in the group while keeping the box size along the in-plane directions unchanged. The effects of strains on cross-plane lattice thermal conductance are shown in Fig. 3(b). It can be observed that κ_L increases monotonically with compressive (negative) strains whereas decreases with tensile (positive) strains. When a 5.2% compressive strain is applied, the thermal conductivity can be enhanced by a high ratio of 78.2%. While with 5.4% tensile strain, κ_L decreases by 59.5%. The predicted results have similar trends with those of coupling strength and coincide well with previous studies of bulk argon systems.[66, 67] Based on the theorems mentioned above, the SED of the bilayers with tensile and compressive strains are evaluated, which are depicted in Fig. S7. It can be observed that applying tensile strain will drop the frequency of the phonon mode at the Γ point, while introducing the compressive strain can lead to the higher phonon frequency. This phenomenon is similar to the result of the bilayer with $\chi = 2$. The phonon relaxation times of bilayer under tensile and compressive strains are shown in Fig. S8. In contrast with the pristine bilayer, the phonon relaxation time will be decreased or increased by applying the tensile or compressive strains. The corresponding average phonon relaxation times are 1.703 and 1.772 ps, respectively, which will reveal the fact that tensile strain can decline the thermal conductivity of bilayer while compressive strain is able to elevate the thermal conductivity. The same 10×10.2 (x×y) nm^2 bilayer system is used to demonstrate the effects of strain on energy transmission at the interface and the results are shown in Fig. S9. Similar to the effect of coupling strength, it can be observed that when the system is under tensile strains, the time it takes for temperature convergence is longer compared to pristine and compress cases.

To help analyze the calculated results, the interlayer interaction strength is derived from the second derivative of LJ potential with respect to layer distance as shown in Fig. 3(c). The interaction strength decreases monotonically with increasing strains, which concurs with the thermal conductivity variations.

It is worth noting that compressive strain has a steeper slope of −5.21 compared to −2.69 from tensile strain, indicating that the former has a much larger impact on the calculated thermal conductivity. Phonon power spectra analyses are also performed to further understand the results. Figure S2 shows the computed phonon spectra of the MLS at thermal equilibrium. From the kinetic theory, the thermal conductivity κ_L can be expressed as $\kappa_L = \sum_i C_i v_i L_i$, where the subscript i denotes the ith phonon mode, C_i is the specific heat, v_i is group velocity and L_i is phonon MFP. It can be observed from Fig. S10(a) that an apparent redshift of the major peaks occurred when the tensile strain was applied. The redshift of the higher frequency peaks reduces the phonon group velocities and results in reduced thermal conductivity according to the classical lattice thermal transport theory.[68] The reduced v_i renders less contribution from the phonon couplings to the interfacial heat flux, leading to higher thermal contact resistance between stanene layers, and lower lattice thermal conductivity. The compressive strain can enhance force constant between interlayer LJ interaction, and causing the blue shift of the major peaks in the PDOS as shown in Fig. S10 (a). To quantitatively prove this point, the phonon power spectra of two neighboring stanene layers with zero, compressive and tensile strains are calculated and presented separately in Figs. S2 (b), (c) and (d).

Based on the above discussions, it is clearly shown that all impact factors could affect the calculated thermal conductivity. In order to obtain an κ_L value for new combinations of layer number, system temperature, interlayer coupling strength and external strain, new MD simulations need to be performed from scratch. To address this issue, a data-driven approach can be applied to directly describe the correlations between different impact factors and the predicted thermal conductivity. There are various hyperparameters in an ANN that can affect its performance, *e.g.* activation function, regularization type, learning rate, depth and width of the neural network. While it is impossible to explore all combinations of hyperparameters, emphases could be given to parameters that play dominant roles, such as the number of layers and neurons in the neural network. In this work, 9 different ANN structures from 1 to 3 layers and 10 to 30 neurons per layer are explored. High-throughout computations are performed to generate the training and test dataset. A total number of 2700 cases are calculated, of which 75% is used for model training and 25% for testing. For ANN, a highly skewed feature space could lead to slow convergence and deteriorated training result. Therefore, before feeding the data into the neural network, all feature values are normalized between 0 and 1. To be consistent, the same normalization is applied to the target value. To preserve the most important feature, Pearson's correlation among all values is explored and the results are shown in Fig. 4. It can be observed that the interlayer coupling strength plays a dominant role compared to other factors with a coefficient value of 0.53. Stratified splitting is used to separate the training and testing dataset based on coupling strength.

The predicted thermal conductivity value from different ANN structures are shown in Fig. 5. The rectified linear unit activation function is used in all hidden layers. The limited-memory Broyden–Fletcher–Goldfarb–Shanno algorithm is used for all model optimizations. The best prediction results are given by the 2-layer ANN with 30 neurons in each layer. The calculated MSE for each model is listed in Table 2. It can be observed that for the same number of layers, the model performance increases with the growing number of neurons. However, the performance could decrease when the neural network becomes deeper. This is caused by the relatively simple correlations among the input features and the target value. Thus, introducing more nonlinearity with extra layers will not further benefit the generalization performance. The trained ANN model can be used to make new predictions within a fraction of a second and saves enormous computational time. The generalization performance of a ML model depends on the data instances fed into the model during training. In this work, batch learning is used instead of on-line learning, which suggests that the training dataset and the feature ranges are fixed. The trained model can be used to predict new κ values when the input features are within the ranges of those in the training dataset. The network could give false results when random feature values are given. On the other hand, the ANN model can be trained to predict other 2D materials given corresponding training data. For instance, in the work, the thermal conductivity of multi-layer stanene are fed into the ANN for model training. Once trained, the model can be used to predict the thermal conductivity of unknown input parameters. To predict κ of other 2D materials such as graphene, phosphorene or hexagonal boron nitride, the ANN models need to re-trained with corresponding training data. It is possible to obtain a comprehensive model which can be used on different types of 2D materials. In that case, the material type becomes one of the feature values. To obtain such a model, an enormous amount of computations needs to be performed.

4. Conclusions

A data-driven approach based on machine learning and high-throughput computation is exemplified in this work to investigate the thermal conductivity in multilayer stanene. The effects of several modulators, such as layer number, system temperature, interlayer coupling strength and tensile strain are explored to accurately gauge its potential as novel thermoelectric materials. Nine different ANN structures are trained to directly model the correlations between different impact factors and the predicted thermal conductivity. The best performance is given by the 2-layer ANN with 30 neurons in each layer. The trained model can predict the thermal conductivity for new cases without repetitive calculations. It is reported that the calculated κ_L values in the cross-plane direction can be greatly diminished with reduced layer number, increased temperature, weakened coupling strength or enlarged tensile strains. The maximum reduction of the predicted κ_L can amount to 80.4%, 73%, 86.7% and 66.6% respectively for the abovementioned modulators. The weakened thermal conductance and phonon couplings are observed with detailed PDOS analyses. An apparent redshift of major peaks occurs when the compressive strains shifted to tensile strains. The PDOS overlap area between neighboring stanene layers is also reduced when tensile strain is applied. The significant decrease of lattice thermal conductivity suggests that MLS could be a promising thermoelectric nanomaterial that can push the upper limit of its *ZT* values.

ACKNOWLEDGEMENT

This work is completed utilizing the Holland Computing Center of the University of Nebraska, which receives support from the Nebraska Research Initiative. X. Wang gratefully acknowledge the support from the National Natural Science Foundation of China (No. 51806123), the Natural Science Foundation of Shandong Province, China (No. ZR2018BEE025), the Guangdong Basic and Applied Basic Research Foundation, China (No. 2020A1515010686) and the China Postdoctoral Science Foundation (No. 2018M642654).

References

[1] D. Castelvecchi, Machine learning comes up against unsolvable problem, Nature, 565(7739) (2019) 277-277.

[2] Z. Ghahramani, Probabilistic machine learning and artificial intelligence, Nature, 521(7553) (2015) 452-459.

[3] D. Wong, S. Yip, Machine learning classifies cancer, Nature, 555(7697) (2018) 446-447.

[4] Y. Hong, B. Hou, H. Jiang, J. Zhang, Machine learning and artificial neural network accelerated computational discoveries in materials science, 10(3) (2020) e1450.

[5] H. Wei, S. Zhao, Q. Rong, H. Bao, Predicting the effective thermal conductivities of composite materials and porous media by machine learning methods, International Journal of Heat and Mass Transfer, 127 (2018) 908-916.

[6] H. Yang, Z. Zhang, J. Zhang, X.C. Zeng, Machine learning and artificial neural network prediction of interfacial thermal resistance between graphene and hexagonal boron nitride, Nanoscale, 10(40) (2018) 19092-19099.

[7] J. Wang, C. Li, S. Shin, H. Qi, Accelerated Atomic Data Production in Ab Initio Molecular Dynamics with Recurrent Neural Network for Materials Research, The Journal of Physical Chemistry C, 124(27) (2020) 14838-14846.

[8] B. Mortazavi, E.V. Podryabinkin, S. Roche, T. Rabczuk, X. Zhuang, A.V. Shapeev, Machine-learning interatomic potentials enable first-principles multiscale modeling of lattice thermal conductivity in graphene/borophene heterostructures, Materials Horizons, (2020).

[9] B. Mortazavi, F. Shojaei, M. Shahrokhi, M. Azizi, T. Rabczuk, A.V. Shapeev, X. Zhuang, Nanoporous C3N4, C3N5 and C3N6 nanosheets; novel strong semiconductors with low thermal conductivities and appealing optical/electronic properties, Carbon, 167 (2020) 40-50.

[10] B. Mortazavi, I.S. Novikov, E.V. Podryabinkin, S. Roche, T. Rabczuk, A.V. Shapeev, X. Zhuang, Exploring phononic properties of two-dimensional materials using machine learning interatomic potentials, Applied Materials Today, 20 (2020) 100685.

[11] B. Mortazavi, E.V. Podryabinkin, I.S. Novikov, S. Roche, T. Rabczuk, X. Zhuang, A.V. Shapeev, Efficient machine-learning based interatomic potentialsfor exploring thermal conductivity in two-dimensional materials, Journal of Physics: Materials, 3(2) (2020) 02LT02.

[12] C. Mangold, S.D. Chen, G. Barbalinardo, J. Behler, P. Pochet, K. Termentzidis, Y. Han, L. Chaput, D. Lacroix, D. Donadio, Transferability of neural network potentials for varying stoichiometry: Phonons and thermal conductivity of MnxGey compounds, J Appl Phys, 127(24) (2020).

[13] R. Li, E. Lee, T. Luo, A unified deep neural network potential capable of predicting thermal conductivity of silicon in different phases, Mater Today Phys, 12 (2020).

[14] C.Z. Zhang, Q. Sun, Gaussian approximation potential for studying the thermal conductivity of silicene, J Appl Phys, 126(10) (2019).

[15] H. Chan, K. Sasikumar, S. Srinivasan, M. Cherukara, B. Narayanan, S.K.R.S. Sankaranarayanan, Machine learning a bond order potential model to study thermal transport in WSe2 nanostructures, Nanoscale, 11(21) (2019) 10381-10392.

[16] X.K. Gu, C.Y. Zhao, Thermal conductivity of single-layer MoS2(1-x)Se2x alloys from molecular dynamics simulations with a machine-learning-based interatomic potential, Comp Mater Sci, 165 (2019) 74-81.

[17] Y. Xu, Z. Gan, S.-C. Zhang, Enhanced Thermoelectric Performance and Anomalous Seebeck Effects in Topological Insulators, Physical Review Letters, 112(22) (2014) 226801.

[18] Y. Xu, P. Tang, S.-C. Zhang, Large-gap quantum spin Hall states in decorated stanene grown on a substrate, Physical Review B, 92(8) (2015) 081112.

[19] F. Matusalem, M. Marques, L.K. Teles, F. Bechstedt, Stability and electronic structure of two-dimensional allotropes of group-IV materials, Physical Review B, 92(4) (2015) 045436.

[20] Y. Ohtsubo, P. Le Fèvre, F. Bertran, A. Taleb-Ibrahimi, Dirac Cone with Helical Spin Polarization in Ultrathin $\ensuremath{\alpha}$-Sn(001) Films, Physical Review Letters, 111(21) (2013) 216401.

[21] F.-f. Zhu, W.-j. Chen, Y. Xu, C.-l. Gao, D.-d. Guan, C.-h. Liu, D. Qian, S.-C. Zhang, J.-f. Jia, Epitaxial growth of two-dimensional stanene, Nat Mater, 14(10) (2015) 1020-1025.

[22] J. Wang, Y. Xu, S.-C. Zhang, Two-dimensional time-reversal-invariant topological superconductivity in a doped quantum spin-Hall insulator, Physical Review B, 90(5) (2014) 054503.

[23] Y. Hong, J. Zhang, X.C. Zeng, Monolayer and Bilayer Polyaniline C3N: Two-Dimensional Semiconductors with High Thermal Conductivity, Nanoscale, 10 (2018) 4301-4310.

[24] Y. Hong, M.G. Ju, J. Zhang, X.C. Zeng, Phonon thermal transport in a graphene/MoSe2 van der Waals heterobilayer, Physical Chemistry Chemical Physics, 20(4) (2018) 2637-2645.

[25] X. Wang, M. Wang, Y. Hong, Z. Wang, J. Zhang, Coherent and incoherent phonon transport in a graphene and nitrogenated holey graphene superlattice, Physical Chemistry Chemical Physics, 19(35) (2017) 24240-24248.

[26] Y. Hong, J. Zhang, X.C. Zeng, Thermal contact resistance across a linear heterojunction within a hybrid graphene/hexagonal boron nitride sheet, Physical Chemistry Chemical Physics, 18(35) (2016) 24164-24170.

[27] H. Yang, Z. Zhang, J. Zhang, X.C. Zeng, Machine Learning and Artificial Neural Network Prediction of Interfacial Thermal Resistance between Graphene and Hexagonal Boron Nitride, Nanoscale, 10 (2018) 19092-19099

[28] L.-D. Zhao, S.-H. Lo, Y. Zhang, H. Sun, G. Tan, C. Uher, C. Wolverton, V.P. Dravid, M.G. Kanatzidis, Ultralow thermal conductivity and high thermoelectric figure of merit in SnSe crystals, Nature, 508(7496) (2014) 373-377.

[29] A.S. Nissimagoudar, A. Manjanath, A.K. Singh, Diffusive nature of thermal transport in stanene, Phys Chem Chem Phys, 18(21) (2016) 14257-14263.

[30] B. Peng, H. Zhang, H. Shao, Y. Xu, X. Zhang, H. Zhu, Low lattice thermal conductivity of stanene, Scientific Reports, 6 (2016) 20225.

[31] M.J. Cherukara, B. Narayanan, A. Kinaci, K. Sasikumar, S.K. Gray, M.K.Y. Chan, S.K.R.S. Sankaranarayanan, Ab Initio-Based Bond Order Potential to Investigate Low Thermal Conductivity of Stanene Nanostructures, The Journal of Physical Chemistry Letters, 7(19) (2016) 3752-3759.

[32] S. Plimpton, Fast Parallel Algorithms for Short-Range Molecular Dynamics, Journal of Computational Physics, 117(1) (1995) 1-19.

[33] J. Wu, H. Wen, H. Shi, C. Chen, B. Huang, Y. Wei, M. Li, Interface thermal conductance in silicene and stanene monolayer:A molecular dynamics study, Superlattices and Microstructures, 130 (2019) 258-266.

[34] S. Das, S. Mojumder, T. Rakib, M.M. Islam, M. Motalab, Atomistic insights into mechanical and thermal properties of stanene with defects, Physica B: Condensed Matter, 553 (2019) 127-136.

[35] M. Noshin, A.I. Khan, S. Subrina, Thermal transport characterization of stanene/silicene heterobilayer and stanene bilayer nanostructures, Nanotechnology, 29(18) (2018) 185706.

[36] Y. Hong, C. Zhu, M. Ju, J. Zhang, X.C. Zeng, Lateral and flexural phonon thermal transport in graphene and stanene bilayers, Physical Chemistry Chemical Physics, 19(9) (2017) 6554-6562.

[37] M.J. Cherukara, B. Narayanan, A. Kinaci, K. Sasikumar, S.K. Gray, M.K.Y. Chan, S.K.R.S. Sankaranarayanan, Ab Initio-Based Bond Order Potential to Investigate Low Thermal Conductivity of Stanene Nanostructures, J Phys Chem Lett, 7(19) (2016) 3752-3759.

[38] A.I. Khan, R. Paul, S. Subrina, Characterization of thermal and mechanical properties of stanene nanoribbons: a molecular dynamics study, Rsc Adv, 7(80) (2017) 50485-50495.

[39] A.K. Rappe, C.J. Casewit, K.S. Colwell, W.A. Goddard, W.M. Skiff, UFF, a full periodic table force field for molecular mechanics and molecular dynamics simulations, Journal of the American Chemical Society, 114(25) (1992) 10024-10035.

[40] F. Müller-Plathe, A simple nonequilibrium molecular dynamics method for calculating the thermal conductivity, The Journal of Chemical Physics, 106(14) (1997) 6082-6085.

[41] G. Balasubramanian, I.K. Puri, M.C. Bohm, F. Leroy, Thermal conductivity reduction through isotope substitution in nanomaterials: predictions from an analytical classical model and nonequilibrium molecular dynamics simulations, Nanoscale, 3(9) (2011) 3714-3720.

[42] A. Bagri, S.-P. Kim, R.S. Ruoff, V.B. Shenoy, Thermal transport across Twin Grain Boundaries in Polycrystalline Graphene from Nonequilibrium Molecular Dynamics Simulations, Nano Letters, 11(9) (2011) 3917-3921.

[43] M. Hu, D. Poulikakos, Si/Ge Superlattice Nanowires with Ultralow Thermal Conductivity, Nano Letters, 12(11) (2012) 5487-5494.

[44] J. Zhang, X. Wang, Thermal transport in bent graphene nanoribbons, Nanoscale, 5(2) (2013) 734-743.

[45] J. Zhang, X. Wang, H. Xie, Phonon energy inversion in graphene during transient thermal transport, Physics Letters A, 377(9) (2013) 721-726.

[46] J. Zhang, X. Wang, H. Xie, Co-existing heat currents in opposite directions in graphene nanoribbons, Physics Letters A, 377(41) (2013) 2970-2978.

[47] J.A. Thomas, J.E. Turney, R.M. Iutzi, C.H. Amon, A.J.H. McGaughey, Predicting phonon dispersion relations and lifetimes from the spectral energy density, Physical Review B, 81(8) (2010) 081411.

[48] J. Zhang, X. Wang, Y. Hong, Q. Xiong, J. Jiang, Y. Yue, Understanding thermal transport in asymmetric layer hexagonal boron nitride heterostructure, Nanotechnology, 28(3) (2017) 035404.

[49] X. Wang, Y. Hong, D. Ma, J. Zhang, Molecular dynamics study of thermal transport in a nitrogenated holey graphene bilayer, Journal of Materials Chemistry C, 5(21) (2017) 5119-5127.

[50] X. Wang, Y. Hong, P. Chan K. L., J. Zhang, Phonon thermal transport in silicene-germanene superlattice: a molecular dynamics study, Nanotechnology, 28(25) (2017) 255403.

[51] Z. Jingchao, W. Xinyu, H. Yang, X. Qingang, J. Jin, Y. Yanan, Understanding thermal transport in asymmetric layer hexagonal boron nitride heterostructure, Nanotechnology, 28(3) (2017) 035404.

[52] W. Xu, G. Zhang, B. Li, Interfacial thermal resistance and thermal rectification between suspended and encased single layer graphene, Journal of Applied Physics, 116(13) (2014) 134303.

[53] Z. Wang, T. Feng, X. Ruan, Thermal conductivity and spectral phonon properties of freestanding and supported silicene, Journal of Applied Physics, 117(8) (2015) 084317.

[54] Y. Hong, J. Zhang, X. Huang, X.C. Zeng, Thermal conductivity of a two-dimensional phosphorene sheet: a comparative study with graphene, Nanoscale, 7(44) (2015) 18716-18724.

[55] Y. Ni, Y. Chalopin, S. Volz, Significant thickness dependence of the thermal resistance between few-layer graphenes, Applied Physics Letters, 103(6) (2013) 061906.

[56] P.K. Schelling, S.R. Phillpot, P. Keblinski, Comparison of atomic-level simulation methods for computing thermal conductivity, Phys Rev B, 65(14) (2002) 144306.

[57] J. Chen, J.H. Walther, P. Koumoutsakos, Strain Engineering of Kapitza Resistance in Few-Layer Graphene, Nano Letters, 14(2) (2014) 819-825.

[58] Z. Wei, Z. Ni, K. Bi, M. Chen, Y. Chen, Interfacial thermal resistance in multilayer graphene structures, Physics Letters A, 375(8) (2011) 1195-1199.

[59] Y.-Y. Zhang, Q.-X. Pei, J.-W. Jiang, N. Wei, Y.-W. Zhang, Thermal conductivities of single- and multi-layer phosphorene: a molecular dynamics study, Nanoscale, 8(1) (2016) 483-491.

[60] J. Zhang, Y. Hong, X. Wang, Y. Yue, D. Xie, J. Jiang, Y. Xiong, P. Li, Phonon Thermal Properties of Transition-Metal Dichalcogenides MoS2 and MoSe2 Heterostructure, The Journal of Physical Chemistry C, 121(19) (2017) 10336-10344.

[61] Y. Hong, J. Zhang, X.C. Zeng, Interlayer thermal conductance within a phosphorene and graphene bilayer, Nanoscale, 8(46) (2016) 19211-19218.

[62] J. Zhang, Y. Hong, M. Liu, Y. Yue, Q. Xiong, G. Lorenzini, Molecular dynamics simulation of the interfacial thermal resistance between phosphorene and silicon substrate, International Journal of Heat and Mass Transfer, 104 (2017) 871-877.

[63] J.-H. Zou, Z.-Q. Ye, B.-Y. Cao, Phonon thermal properties of graphene from molecular dynamics using different potentials, The Journal of Chemical Physics, 145(13) (2016) 134705.

[64] R. Prasher, Acoustic mismatch model for thermal contact resistance of van der Waals contacts, Applied Physics Letters, 94(4) (2009) 041905.

[65] R. Jaeger, J.B. Lagowski, I. Manners, G.J. Vancso, Ab initio studies on the structure, conformation, and chain flexibility of halogenated poly(thionylphosphazenes), Macromolecules, 28(2) (1995) 539-546.

[66] S. Bhowmick, V.B. Shenoy, Effect of strain on the thermal conductivity of solids, The Journal of Chemical Physics, 125(16) (2006) 164513.

[67] R.C. Picu, T. Borca-Tasciuc, M.C. Pavel, Strain and size effects on heat transport in nanostructures, Journal of Applied Physics, 93(6) (2003) 3535-3539.

[68] L. Shi, Thermal and Thermoelectric Transport in Nanostructures and Low-Dimensional Systems, Nanoscale and Microscale Thermophysical Engineering, 16(2) (2012) 79-116.

[69] W. Zhiyong, L. Biao, L. Chenhan, B. Kedong, Y. Juekuan, C. Yunfei, Cross-plane phonon transport properties of molybdenum disulphide, Journal of Physics D: Applied Physics, 48(46) (2015) 465303.

[70] A. Tolga, K.M. Jeremy, E. Hakan, A new interlayer potential for hexagonal boron nitride, Journal of Physics: Condensed Matter, 28(38) (2016) 385401.

Table and Figures

Table 1. Cross-plane thermal conductivity of popular vdW structures at room temperature.

Group	vdW Structure	κ (W/m·K)
Wei *et al.*[58]	Graphene	11.57
Wei *et al.*[69]	MoS_2	6.6
Akıner *et al.*[70]	Hexagonal boron nitride	1.3
Hong *et al.*	Stanene	0.83
Zhang *et al.*[59]	Phosphorene	0.42

Table 2. Normalized mean square error for different ANN architectures. The column index represents the number of neural layers. The row header represents neurons per layer.

ANN	10	20	30
1	0.008085	0.007825	0.007710
2	0.007990	0.007835	0.007335
3	0.008370	0.008027	0.007498

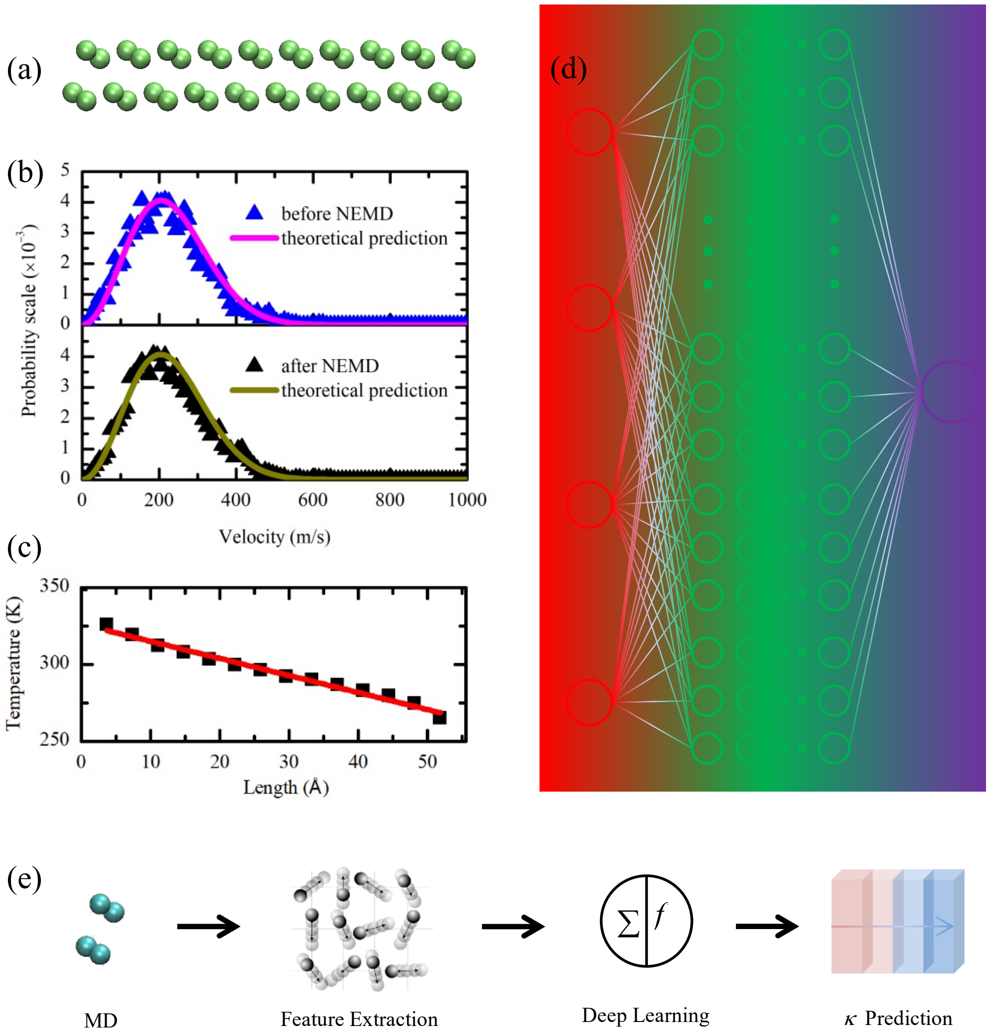

Figure 1. (a) Side view of stacked stanene layers. (b) Velocity distributions of the system before and after the NEMD simulation. (c) Temperature distribution along the heat flux direction at steady state. (d) Schematic of a typical artificial neural network structure. (e) Workflow of a data-driven approach based on high-throughput computation and machine learning.

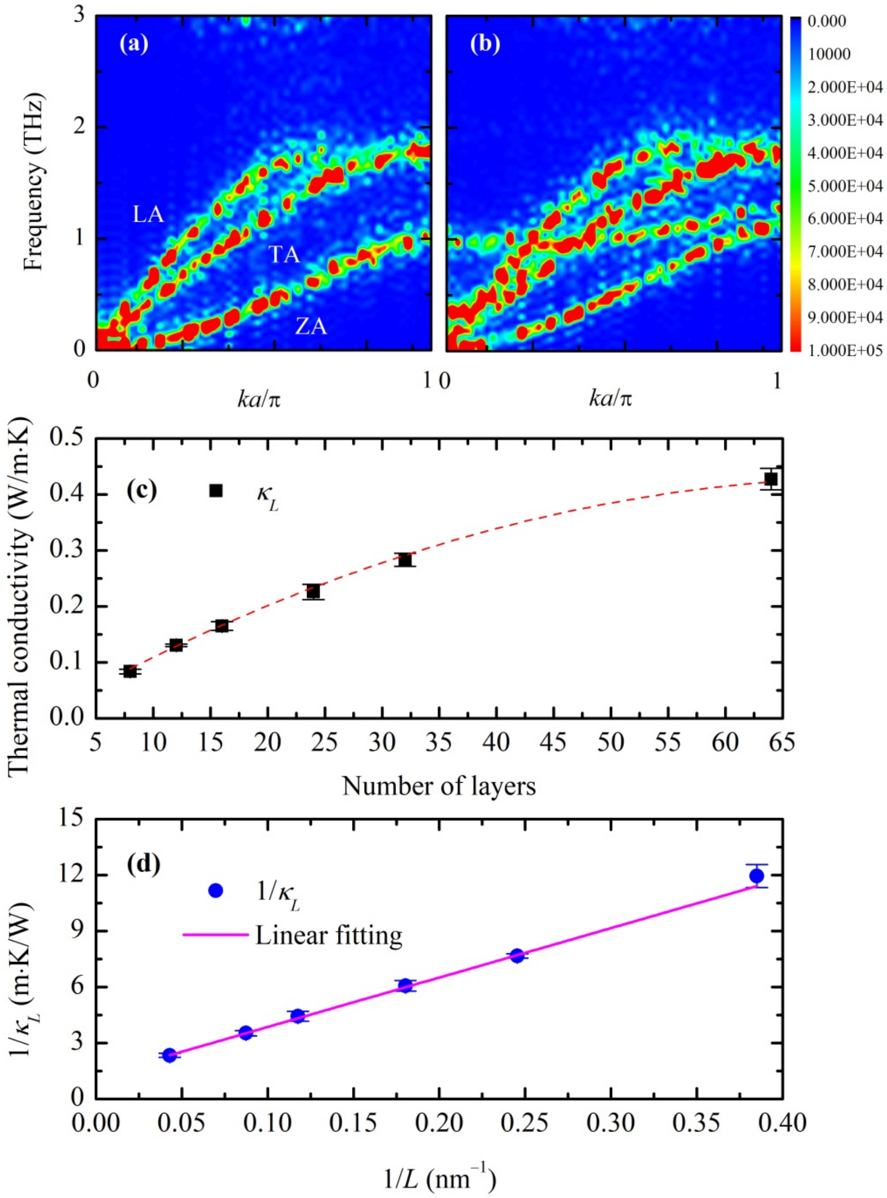

Figure 2. Phonon spectral energy densities of (a) freestanding stanene and (b) supported stanene in a bilayer system. (c) Dependence of cross-plane κ_L with layer number. The red dashed line is plotted for visual aid. (d) Correlation between $1/\kappa_L$ and $1/L$. The pink solid line represents the linear fitting result.

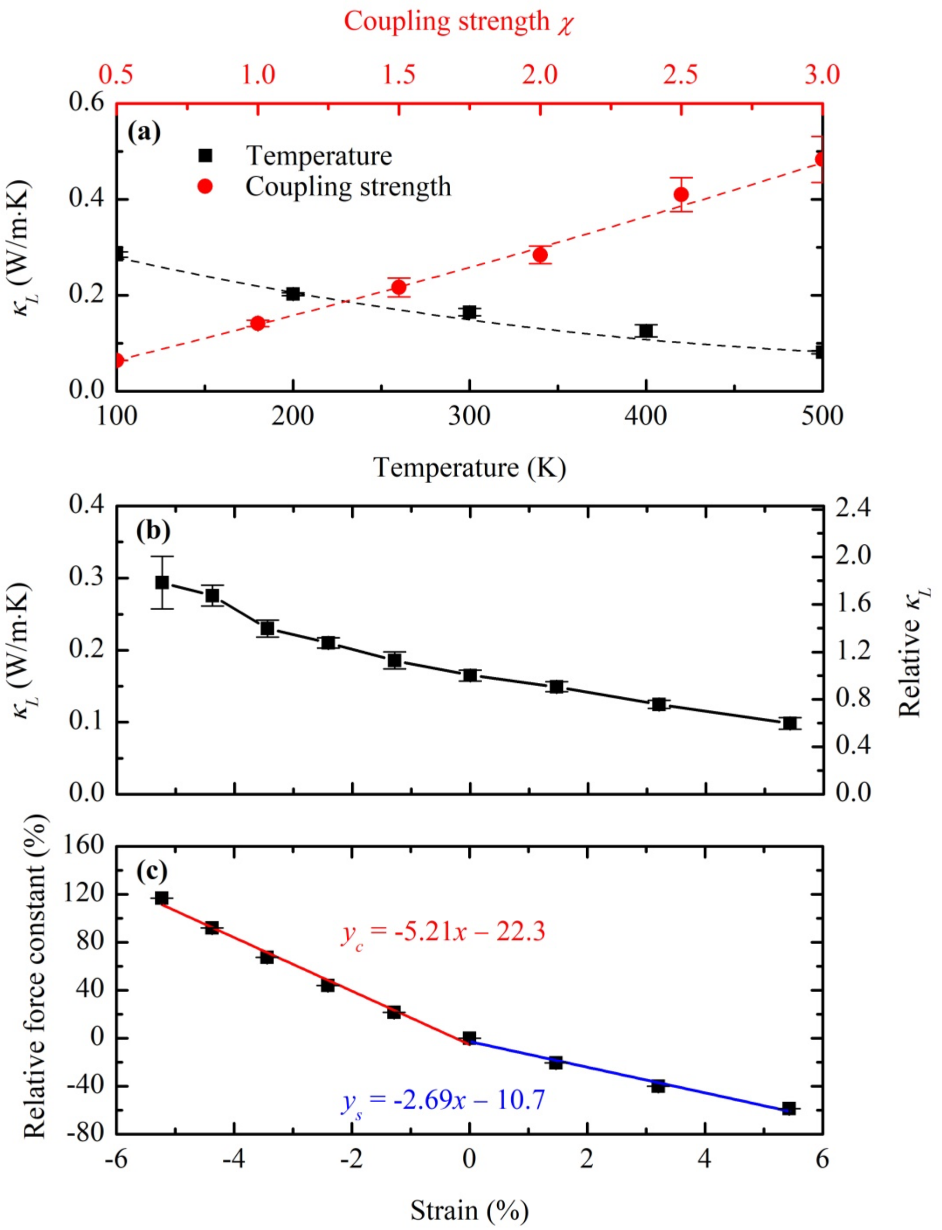

Figure 3. (a)The bottom *x*-axis denotes κ_L dependence with temperature. The top *x*-axis illustrates the effects of LJ coupling strength. (b) Dependence of κ_L with strain. (c) Variations of force constant with compressive and tensile strains. The red solid line is the linear fitting profile for compressive strains, and the blue solid line stands for the fitting results for tensile strains.

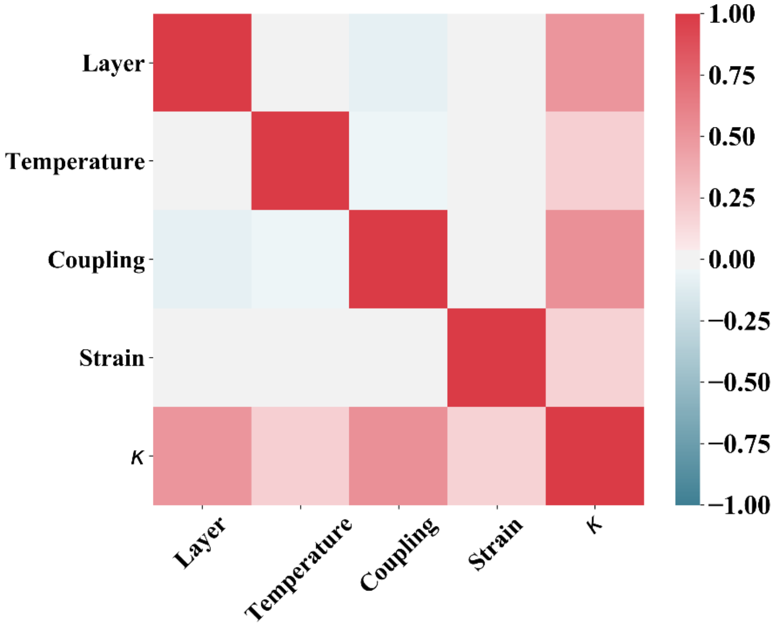

Figure 4. Pearson's correlation coefficients among different features and target values. The coupling strength has the most significant effect on cross-plane thermal conductivity with a coefficient value of 0.53, followed by layer number as the second-largest coefficient of 0.51.

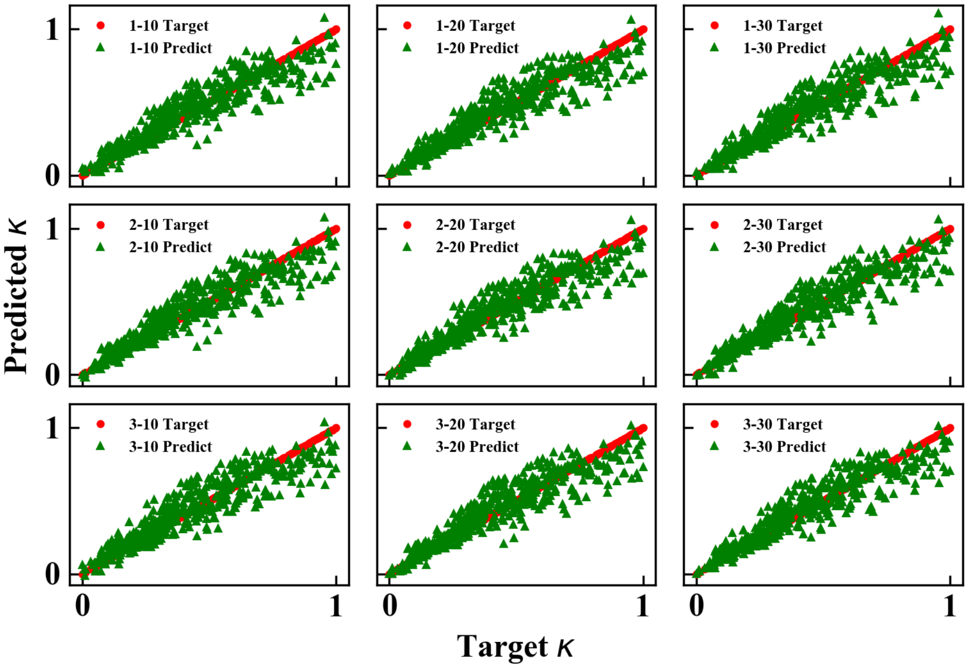

Figure 5. Artificial neural network training results on the cross-plane thermal conductivity *κ*. Two hyperparameters, *i.e.* layer number and neuron per layer are explored. The 2-layer ANN with 30 neurons per layer has the best prediction results with an MSE of 0.0073.